Supplementary Information

Upcycling waste plastic and spent batteries into hierarchical Co/Carbon nanocomposites for high-performance electromagnetic wave absorption

Binghong Lin[1], Kun Zuo[1], Yihong Zheng, Botao Zheng, Mulan Tu, Xiaochuan Chen*, Junxiong Wu*, Xiaoyan Li* and Yuming Chen*

Engineering Research Center of Polymer Green Recycling of Ministry of Education, Fujian Key Laboratory of Pollution Control & Resource Reuse College of Environmental and Resource Sciences and College of Carbon Neutral Modern Industry, Fujian Normal University, Fuzhou, 350117, China.

*Corresponding authors.

E-mail addresses: chenxiaocuan@fjnu.edu.cn (X. Chen), jwuba@fjnu.edu.cn (J. Wu), xiaoyanli1985@126.com (X. Li), yumingc126@126.com (Y. Chen).

[1] These authors contributed equally.

1. Experimental

1.1. Materials

Waste PET plastics [$(C_{10}H_8O_4)_n$], sourced from discarded plastic water bottles, spent $LiCoO_2$ batteries ($LiCoO_2$ purchased from the market), ethanol, and N, N-dimethylformamide (DMF, AR ≥ 99.5%) were supplied by Sinopharm Chemical Reagent Co., Ltd.

1.2. Upcycling of spent $LiCoO_2$ to $CoCl_2$

The recycling of $CoCl_2$ from spent $LiCoO_2$ batteries was illustrated in Fig. S1a. The cathode sheets were separated, leached with an HCl solution, and the resulting leachate was subjected to evaporation and crystallization, yielding a pink powder denoted as recycled $CoCl_2$ (R-$CoCl_2$).

1.3. Upcycling of waste PET to TPA

The process for converting waste PET into terephthalic acid (TPA) was shown in Fig. S1b. Briefly, 5 g of PET was dispersed in 50 mL of ethylene glycol [$(CH_2OH)_2$] and 50 mL deionized water solution under stirring. The mixture was transferred into a stainless-steel autoclave with a polytetrafluoroethylene (PTFE) liner and heated at 200 °C for 8 h in an explosion-proof oven. After cooling, the product was collected by centrifugation, washed several times, and vacuum-dried at 80 °C for 12 h to obtain a white powder, designated as recycled TPA (R-TPA).

1.4. Synthesis of the Co-MOF precursor

The synthesis procedure for the Co-MOF precursor is depicted in Fig. 1a. In a typical process, 1.66 g of R-TPA and 1.3 g of R-$CoCl_2$ were dispersed in 50 mL of DMF under magnetic stirring for 1 h to form a homogeneous pink solution. The solution was then transferred into a PTFE-lined stainless-steel autoclave and heated at 180 °C for 24 h. The resulting product was isolated by centrifugation, washed thoroughly, and vacuum-dried at 80 °C for 12 h to obtain the Co-MOF precursor.

1.5. Synthesis of Co@C and Co@CNT composites

The Co@C and Co@CNT composites were fabricated via annealing and pyrolysis processes. The Co@C composite was prepared by direct pyrolysis of the as-synthesized Co-MOF in a tube furnace under a flowing Ar/H_2 atmosphere. The temperature was raised to 700 °C at a heating rate of 2 °C/min and held for 3 h. For the Co@CNT composites, the Co-MOF precursor was physically mixed with R-TPA at mass ratios of 10 wt% and 15 wt%, followed by co-pyrolysis under identical conditions. The resulting composites were labeled as Co@CNT-10 and Co@CNT-15, respectively.

1.6 Characterization and electromagnetic wave absorption performance

The crystal structure of the prepared composites was analyzed by X-ray diffraction (XRD). Elemental composition and valence states were determined using X-ray photoelectron spectroscopy (XPS). Raman spectroscopy was employed to evaluate the degree of

graphitization in composites. The microstructure and morphology were characterized by scanning electron microscopy (SEM) and transmission electron microscopy (TEM). Specific surface area and pore size distribution were measured with a specific surface area and pore size analyzer (BET). Magnetic properties were examined using a vibrating sample magnetometer (VSM).

To evaluate the electromagnetic wave absorption performance, the composites were uniformly mixed with paraffin at a mass ratio of 23 wt% and pressed into coaxial rings with an outer diameter of 7.0 mm and an inner diameter of 3.04 mm. The complex permittivity and permeability of the rings were measured in the frequency range of 2-18 GHz using a vector network analyzer (VNA) via the coaxial-line method.

1.7 Math formulae and computational methods

Based on the transmission line theory to evaluate EMW absorption performance of the obtained composites, the reflection loss (RL) values of the three composites were calculated at a filler loading of 23 wt%. The EMW absorption capability of absorbing materials is typically expressed by RL, where a smaller RL value indicates stronger attenuation. When the RL value is less than −10 dB, the material absorbs 90% of the incident electromagnetic waves. The EAB defined as the frequency range where RL < −10 dB, is another key metric for assessing EMW absorption performance. The RL values were calculated using the following equations derived from electromagnetic parameters:

$$Z_{in} = Z_0\sqrt{\mu_r/\varepsilon_r}\tan h\cdot\left[j(2\pi f d/c)\times\sqrt{\mu_r\varepsilon_r}\right]\#(1)$$

$$RL = 20\log_{10}\left|\frac{Z_{in}-Z_0}{Z_{in}+Z_0}\right|\#(2)$$

Where Z_{in} is the normalized input impedance of the material, Z_0 is the characteristic impedance of free space (approximately 377 Ω), f is the frequency of the electromagnetic waves, c is the speed of light in free space, and d is the thickness of the absorber layer, ($\varepsilon_r = \varepsilon' - j\varepsilon''$, $\mu_r = \mu' - j\mu''$) are the relative complex permittivity and permeability.[1]

Another factor in evaluating EMW absorption performance is the attenuation constant (α), which indicates the dissipation degree of electromagnetic waves within the material [2,3] attenuation constant is calculated using the following equation:

$$\alpha = \frac{\sqrt{2}\pi f}{c}\sqrt{\left(\mu''\varepsilon'' - \mu'\varepsilon'\right) + \sqrt{\left(\mu''\varepsilon'' - \mu'\varepsilon'\right)^2 + \left(\mu''\varepsilon'' + \mu'\varepsilon'\right)^2}} \#(3)$$

where f is the frequency of the electromagnetic waves, and c is the speed of light.

Based on Debye relaxation theory, the relationship between ε' and ε'' is expressed as follows：

$$\left(\varepsilon' - \frac{\varepsilon_s + \varepsilon_\infty}{2}\right)^2 + \left(\varepsilon''\right)^2 = \left(\frac{\varepsilon_s - \varepsilon_\infty}{2}\right)^2 \#(4)$$

where ε_s is the static dielectric constant, and ε_∞ is the high-frequency dielectric constant.

The relationship between the eddy current coefficient C_0 and frequency assesses the dominant contribution of eddy current loss to the magnetic loss mechanism. If C_0 remains almost constant or shows minimal frequency-dependent fluctuations, eddy current loss serves as the primary magnetic loss mechanism.[4,5] Eddy current loss can be evaluated using the following equation:

$$C_0 = \mu''\left(\mu'\right)^{-2} f^{-1} \#(5)$$

where f is the frequency of the electromagnetic waves.

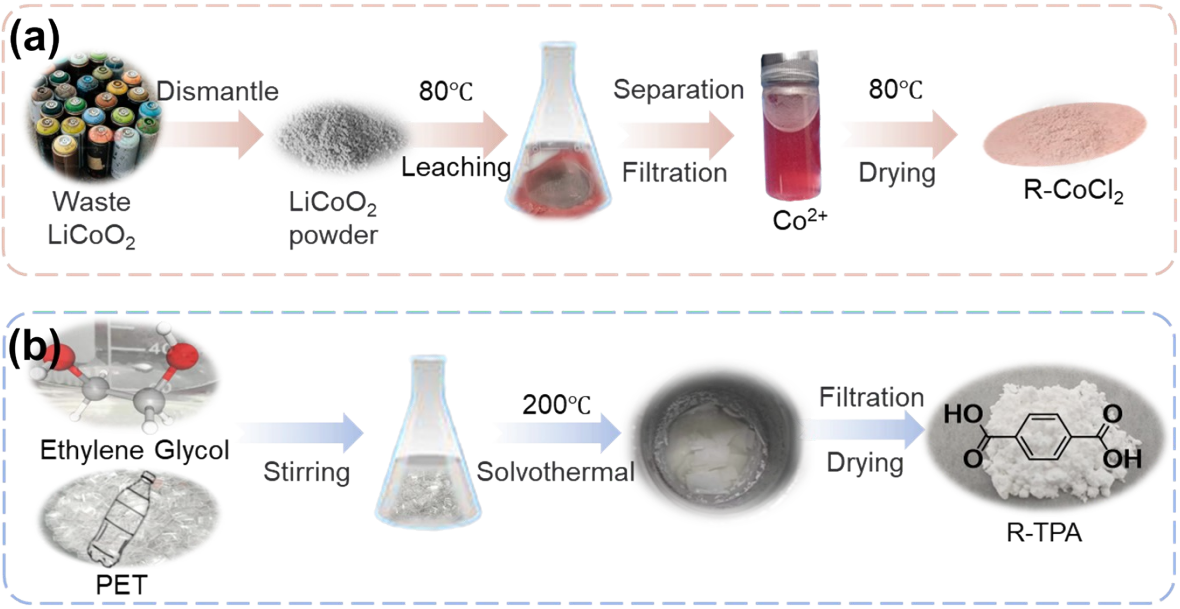

Fig. S1. (a) Recycling waste $LiCoO_2$ to prepare R-$CoCl_2$ and (b) Recycling waste PET to prepare R-TPA.

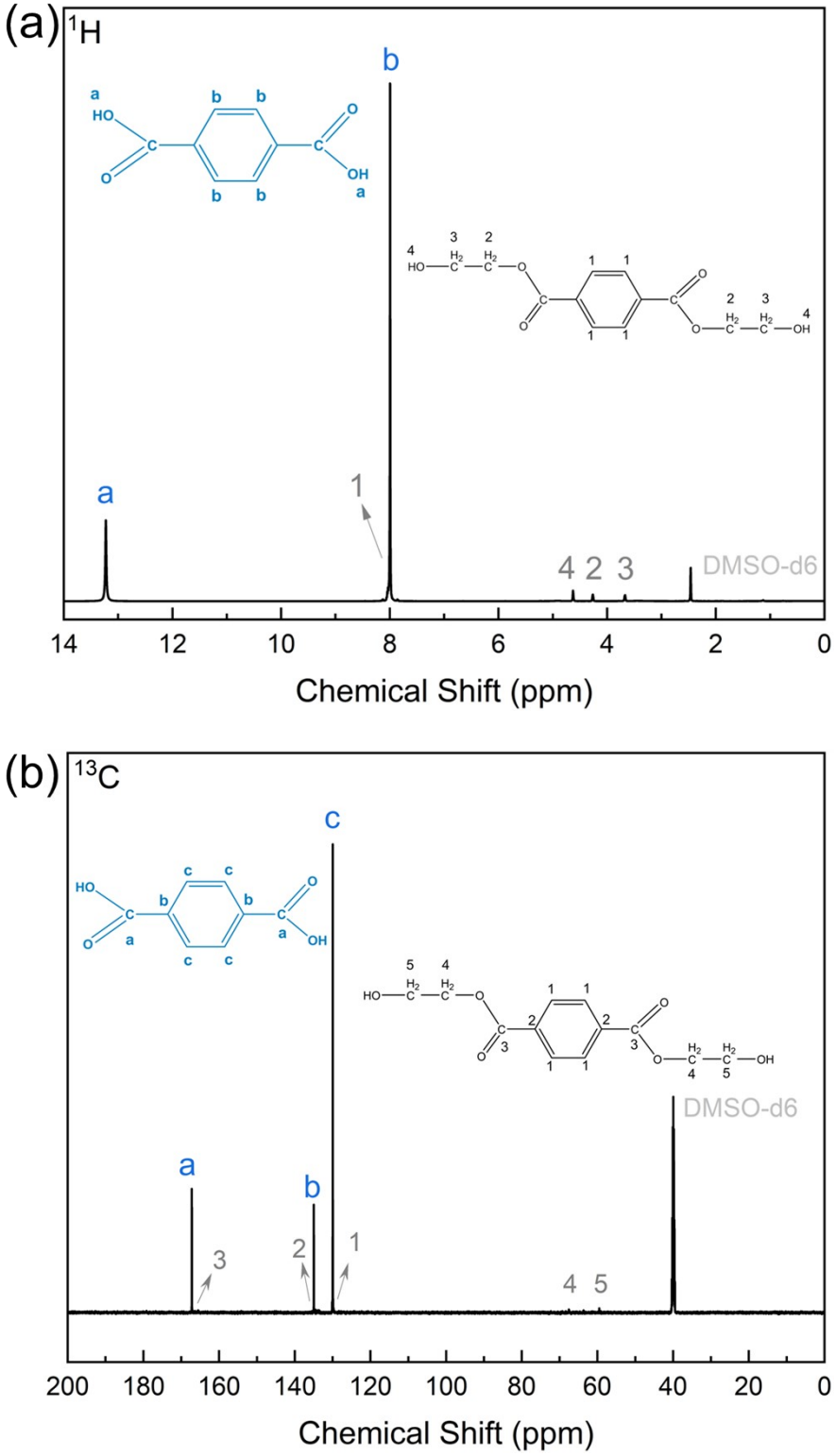

Fig. S2 The recovered terephthalic acid (a)^{1}H-NMR and (b) ^{13}C-NMR in DMSO-d6 solvent. NMR analysis confirms that the recovered TPA is of high purity, with the spectrum showing only a trace residual amount of bis(2-hydroxyethyl) terephthalate (BHET), which indicates a highly efficient recovery and purification process.

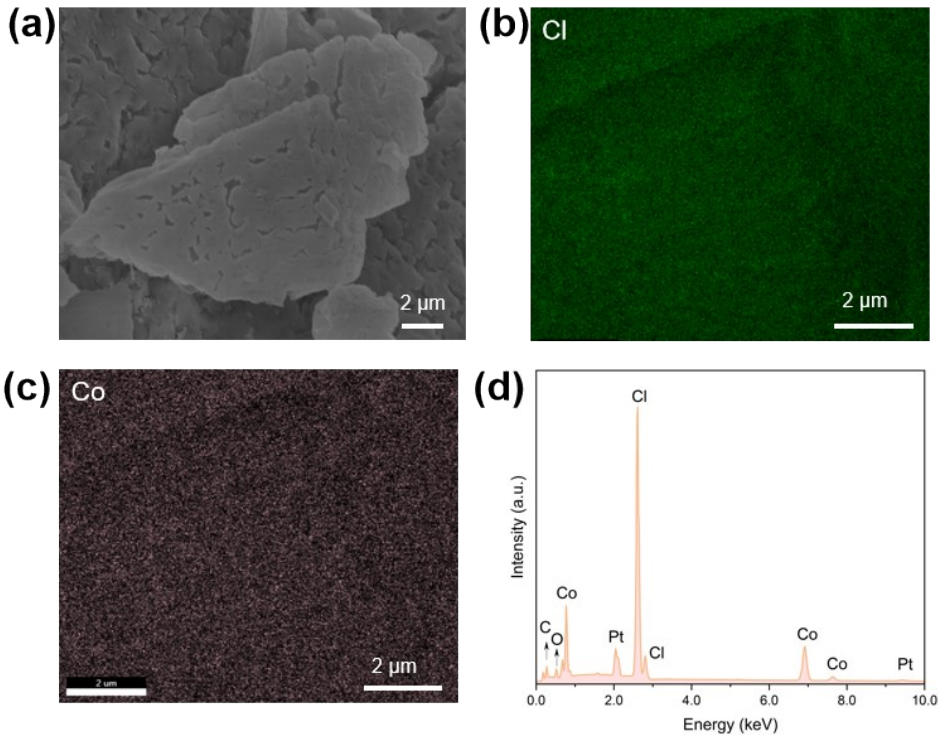

Fig. S3 (a–c) SEM image, the corresponding elemental mapping, and (d) EDS spectrum of the recovered cobalt-based precursor. The signals of C, O, and Pt are primarily attributed to the carbon conductive film and the Pt sputtering layer on the samples. Furthermore, the atomic ratio of Cl to Co in the recycled material is 1.96, which is close to the theoretical value of 2 (see Table S1), confirming the successful recovery of high-purity $CoCl_2$.

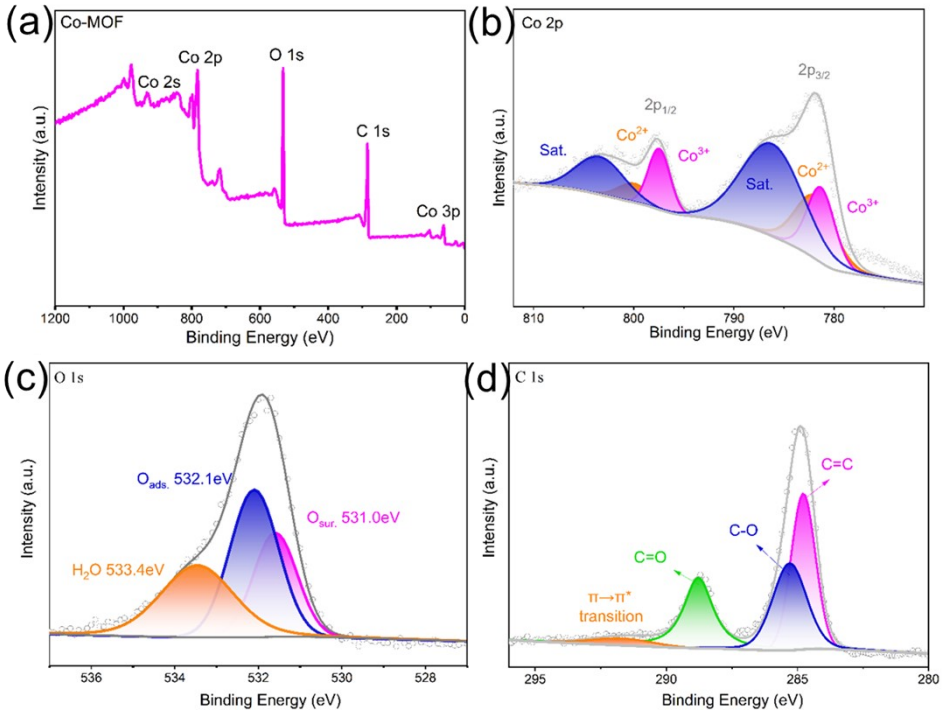

Fig. S4 High-resolution XPS spectra of Co-MOF. (a) survey spectra, (b)Co 2p, (c) O 1s and (d) C 1s. The results clearly indicate the formation of a carboxylate-coordinated Co-MOF framework. Specifically, the Co $2p^{3/2}$ peak appears at approximately 781.2 eV with a pronounced satellite peak, confirming the Co^{2+} oxidation state. The spectral features are characteristic of Co-O coordination with organic linkers and differ distinctly from those of metallic Co or cobalt oxides.

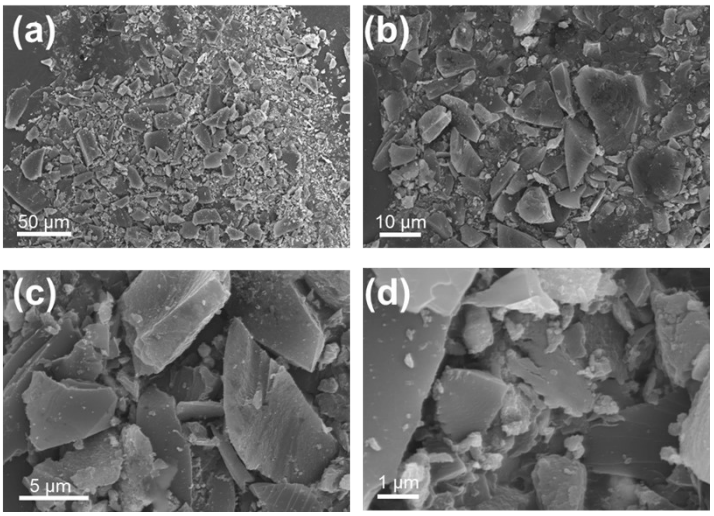

Fig. S5 SEM images of carbonization of R-TPA.

As shown in Fig. 2 f–g, the Co-MOF precursor pyrolyzed alone maintains a layered carbon morphology but does not generate CNTs. In contrast, when co-pyrolyzed with R-TPA, the product exhibits a well-designed hierarchical structure with CNTs grown on carbon nanosheets (Fig. 3). This structural difference can be attributed to the role of R-TPA: as indicated in Fig. S6, R-TPA pyrolysis yields bulk carbon particles. Therefore, during co-pyrolysis, R-TPA serves a dual function: (1) as an additional carbon source for CNT growth, and (2) in conjunction with Co species derived from the MOF, providing the catalytic sites necessary for CNT formation.

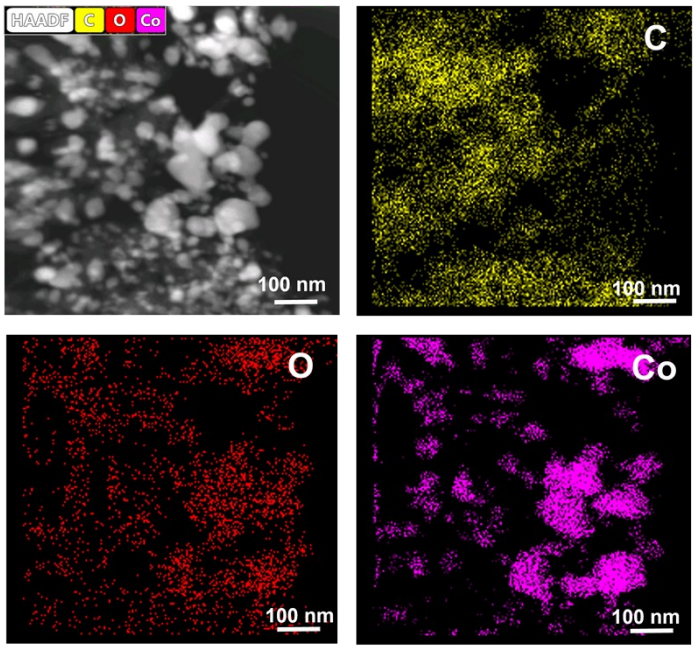

Fig. S6. EDS element mapping of Co@CNT-15.

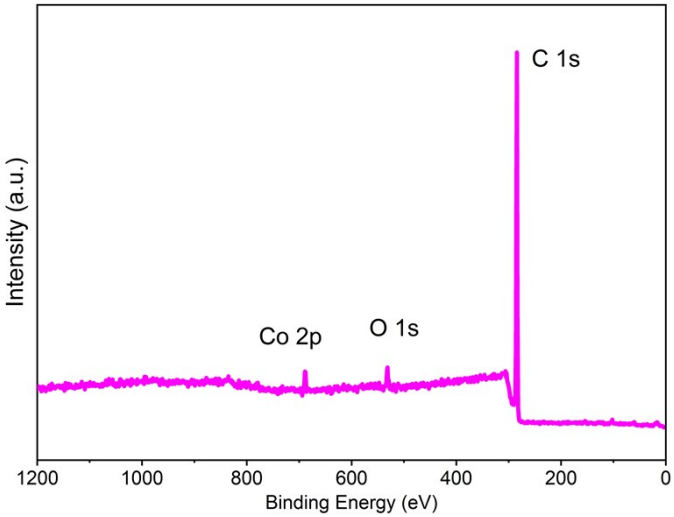

Fig. S7. XPS survey spectrum of Co@CNT-15.

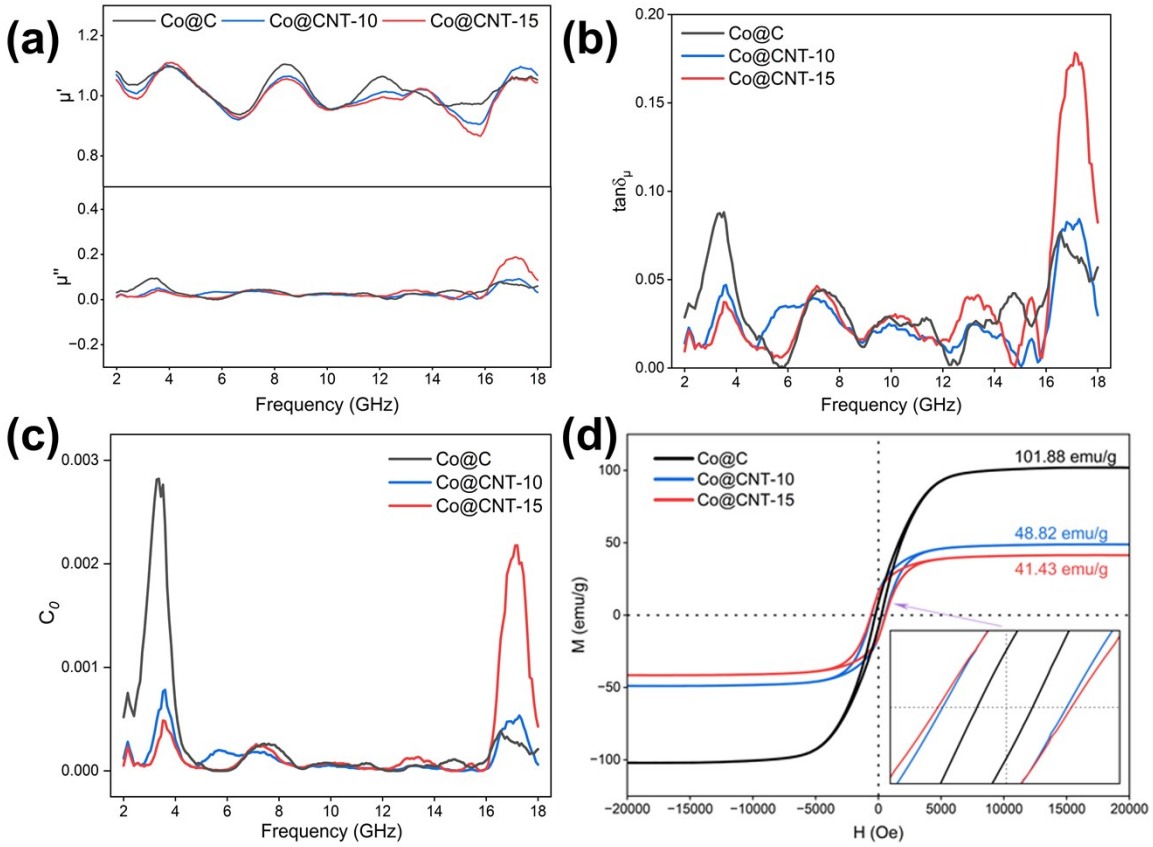

Fig. S8. (a) Complex permeability, (b) Magnetic loss tangent, (c) C_0 values and (d) Hysteresis loops of the obtained composites.

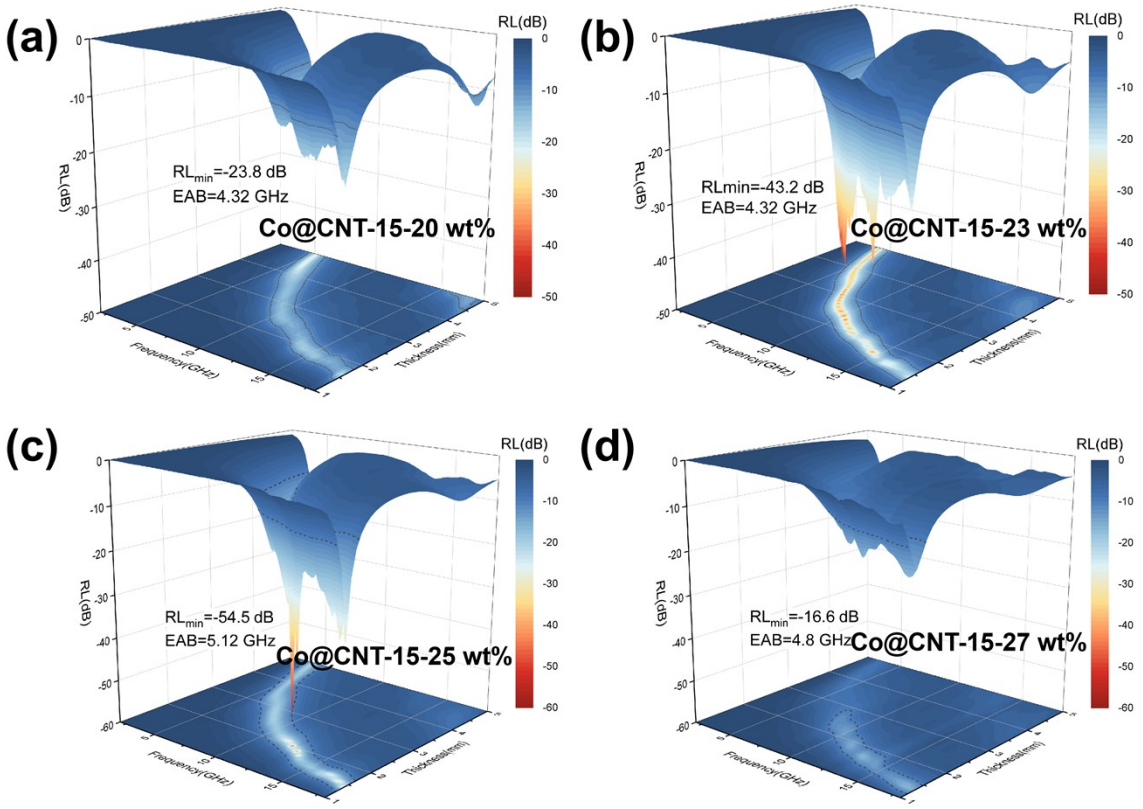

Fig. S9. 3D planar RL plots of Co@CNT-15 at paraffin filling ratios of (a-d) 20 wt%, 23 wt%, 25 wt%, and 27 wt%.

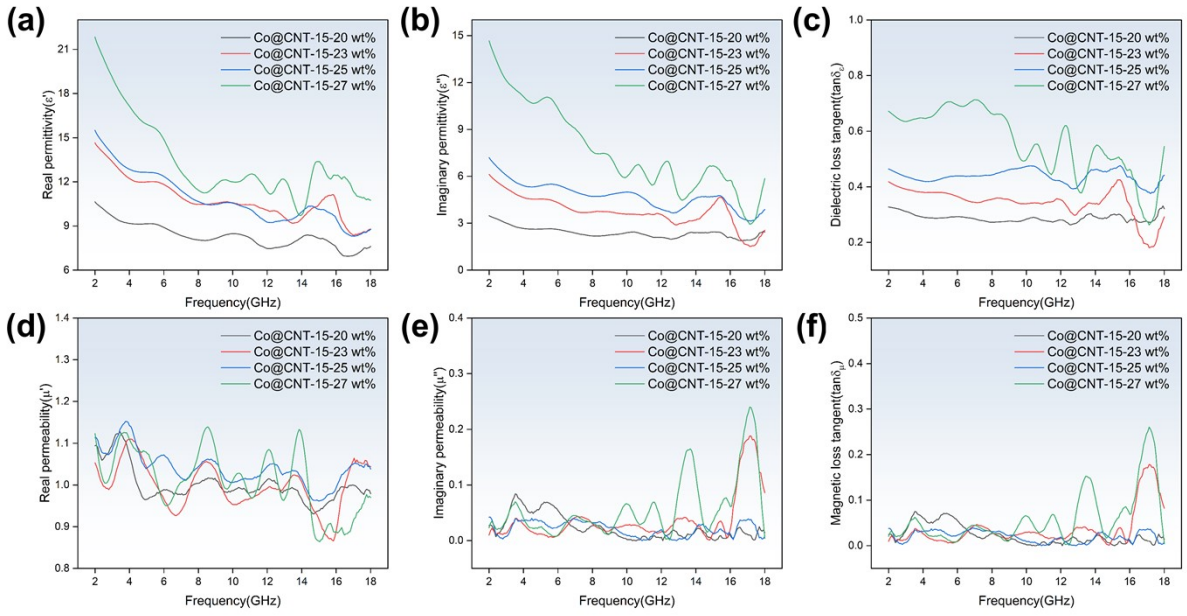

Fig. S10. (a)Real part of permittivity, (b) Imaginary part of permittivity, (c) Dielectric loss tangent, (d) Real part of permeability, (e) Imaginary part of permeability, and (f) Magnetic loss tangent of Co@CNT-15 at paraffin filling ratios of 20 wt%, 23 wt%, 25 wt%, and 27 wt%.

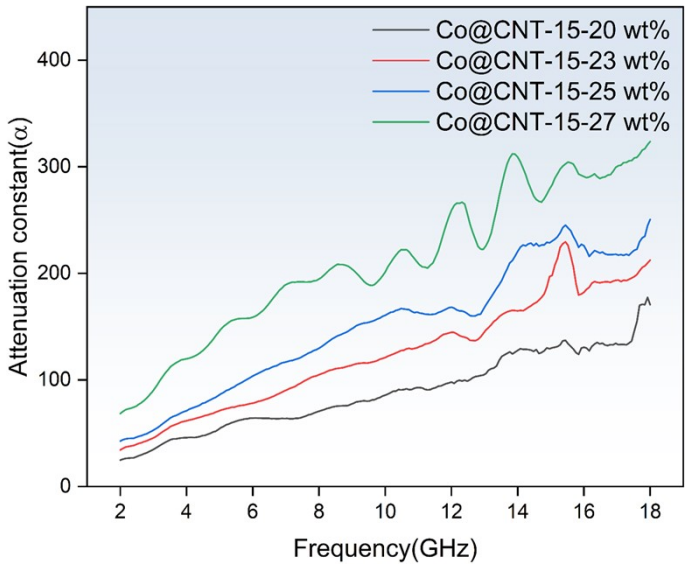

Fig. S11. EMW attenuation constant of the obtained composites at different filler ratios.

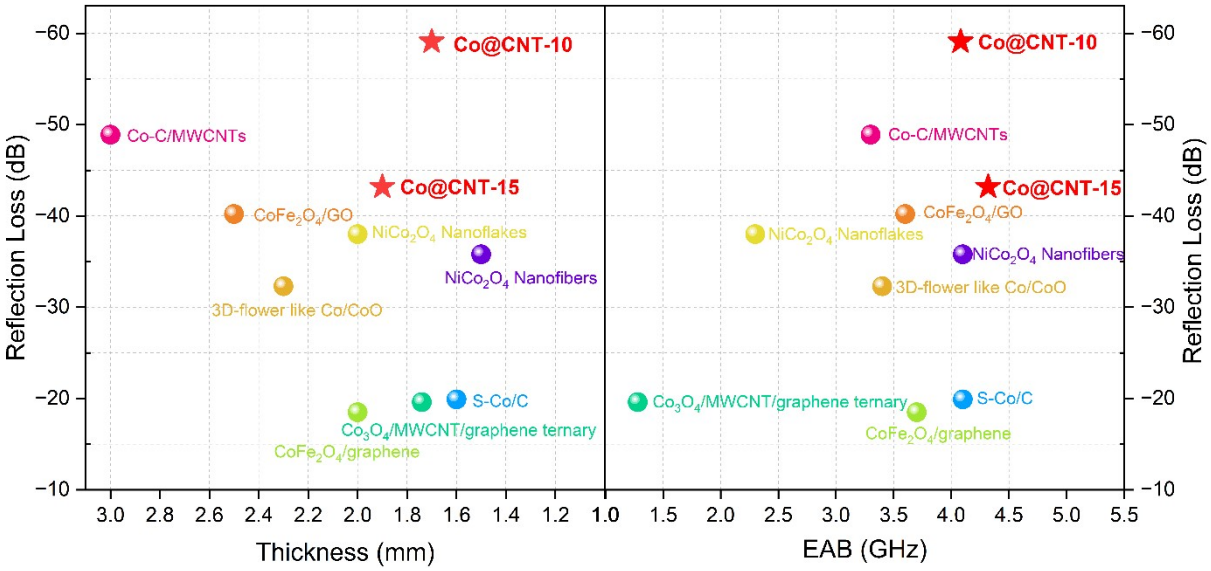

Fig. S12. Comparison of EMW properties among the Co@CNT nanocomposites and other absorbers reported in the references.

Table S1 Elemental analysis of the recycled cobalt-based precursor.

Element	Weight %	Atomic %	Error %
Cl	42.36	40.26	2.79
Co	35.97	20.57	2.86

Table S2. Comparison of EMW absorption properties among the obtained Co/C composites and other materials.

Type	EAB (GHz)	Thickness (mm)	RL_{min} (dB)	Filling ratio (wt. %)	Frequency [RL≤-10dB] (GHz)	Material	References
Cobalt-carbon-based absorbers	**4.08**	**1.70**	**−59.1**	**23**	**4.00—18.0**	**Co@CNT-10**	**This work**
	4.32	**1.90**	**−43.2**	**23**	**3.68—18.0**	**Co@CNT-15**	
	3.40	3.00	−48.9	15	5.90—18.0	Co-C/MWCNTs	6
	4.00	2.30	−32.3	50	9.50—12.0	3D-flower like Co/CoO	7
	3.30	1.74	−19.6	30	8.40—12.0	Co_3O_4/MWCNT/ graphene ternary	8
	3.50	1.60	−19.9	40	8.40—14.2	S-Co/C	9
Alloy and metal oxide-based absorbers	3.70	2.50	−40.2	50	4.40—18.0	$CoFe_2O_4$/GO	10
	4.10	2.00	−18.5	60	11.3—15.0	$CoFe_2O_4$/graphene	11
	2.30	2.00	−38.0	50	4.00—16.0	$NiCo_2O_4$ Nanoflakes	12
	3.60	1.50	−35.8	50	6.20—18.0	$NiCo_2O_4$ Nanofibers	13

References

1 L. Ding, Y. Huang, Z. Xu, J. Yan, X. Liu, T. Li and P. Liu, *Compos. Commun.*, 2020, **21**, 100362.

2 W. Deng, T. Li, H. Li, A. Dang, X. Liu, J. Zhai and H. Wu, *Carbon*, 2023, **206**, 192–200.

3 R. Guo, Q. Zheng, L. Wang, Y. Fan and W. Jiang, *J. Mater. Sci. Technol.*, 2022, **106**, 108–117.

4 P. Jablonski, M. Najgebauer and M. Bereznicki, *Energies*, 2022, **15**, 2869.

5 H. Ohguchi, S. Takigawa and S. Imamori, *IET Electr. Power Appl.*, 2024, **18**, 278–286.

6 Y. Yin, X. Liu, X. Wei, Y. Li, X. Nie, R. Yu and J. Shui, *ACS Appl. Mater. Interfaces*, 2017, **9**, 30850–30861.

7 Y. Li, J. Zhang, Z. Liu, M. Liu, H. Lin and R. Che, *J. Mater. Chem. C*, 2014, **2**, 5216–5222.

8 Z. Guan, J. Jiang, S. Yan, Y. Sun and L. Zhen, *J. Colloid Interface Sci.*, 2020, **561**, 687–695.

9 Y. Lu, Y. Wang, H. Li, Y. Lin, Z. Jiang, Z. Xie, Q. Kuang and L. Zheng, *ACS Appl. Mater. Interfaces*, 2015, **7**, 13604–13611.

10 X. Li, J. Feng, Y. Du, J. Bai, H. Fan, H. Zhang, Y. Peng and F. Li, *J. Mater. Chem. A*, 2015, **3**, 5535–5546.

11 M. Fu, Q. Jiao, Y. Zhao and H. Li, *J. Mater. Chem. A*, 2014, **2**, 735–744.

12 M. Zhou, F. Lu, B. Chen, X. Zhu, X. Shen, W. Xia, H. He and X. Zeng, *Mater. Lett.*, 2015, **159**, 498–501.

13 J. Zhan, Y. Yao, C. Zhang and C. Li, *J. Alloy. Compd.*, 2014, **585**, 240–244.